Kovove Mater. 61 2023 135–143
DOI: 10.31577/km.2023.3.135

Crystal structure, magnetic and thermal properties of the non-stoichiometric alloys $Tb_{0.95}Pd_{2.20}Mn_{0.85}$ and $Dy_{1.00}Pd_{2.15}Mn_{0.85}$

Taras Kovaliuk[1]*, Ross Harvey Colman[1], Barbora Vondráčková[1], Oleksandr Kolomiets[2], Milan Klicpera[1]

[1] *Charles University, Faculty of Mathematics and Physics, Department of Condensed Matter Physics, Ke Karlovu 5, 121 16 Prague 2, Czech Republic*
[2] *Lviv Polytechnic National University, Department of Physics, Bandera Str. 12, 79013 Lviv, Ukraine*

Received 8 February 2023, received in revised form 3 March 2023, accepted 8 March 2023

Abstract

The alloys RNi$_2$Mn and RCo$_2$Mn with R representing the rare earth element are isostructural analogues of the binary Laves phases RNi$_2$, RCo$_2$. We have synthesized the isoelectronic Pd-based RPd$_2$Mn analogues with R = Gd, Tb, and Dy, for the first time. They crystallize in a cubic structure, however, not in the cubic C15 (*Fd-3m*) structure of RNi$_2$Mn, nor the Laves phase' structure. Instead, the crystal lattice is described by the *Im-3m* space group with Tb/Dy, Pd, and Mn atoms randomly distributed over the 2*a* Wyckoff position of the W-type structure (A2, disordered bcc). The magnetization data reveal a standard paramagnetic behavior, with effective magnetic moments strikingly close to those expected for Tb^{3+} and Dy^{3+} free ions, down to 130 K.

K e y w o r d s: $RETM_2$Mn, $RE_{1-y}Pd_{2+x+y}Mn_{1-x}$ alloys, solid solutions, intermetallics, crystal structure, magnetization

1. Introduction

RT_2 Laves phases, where R stands for the rare-earth element and T is the transition element, have attracted considerable and repeated attention. Generally, these Laves phases crystallize in a cubic structure of $MgCu_2$-type (C15, *Fd-3m*) or hexagonal structures of $MgZn_2$-(C14, *P6$_3$/mmc*) or $MgNi_2$-type (C36, *P6$_3$/mmc*), based rather on the principle of the close packing of spherical atoms rather than direction-dependent (covalent) chemical bonding [1]. The empirical rules governing the formation of a Laves phase require the ratio of the atomic radii of R and T atoms to be between 1.05 and 1.67 [2]. However, there are exceptions to the rule. Considering the subject of the present work, we highlight the nominal RPd$_2$ series. Recently, the actual stoichiometry of the majority of the members was determined to be $R_{10}Pd_{21}$, and their crystal structure was identified as monoclinic of $Sm_{10}Pd_{21}$-type (*C2/m*) [3].

RT_2 alloys have been of scientific interest due to their remarkable magnetic properties and application potential. RFe$_2$ alloys exhibit large magnetic anisotropy and magnetostriction/magnetostrain, making them an excellent choice for magnetomechanical actuators and sensors, see [4] and references therein. RAl$_2$ and RCo$_2$ alloys reveal considerable magnetocalorical effects at low temperatures [5, 6], representing suitable materials for hydrogen liquefaction. In RMn$_2$ alloys, the Mn-Mn interatomic distance (critical limit 2.67Å), tightly connected with R atomic radius, determines in which members the manganese ions carry a magnetic moment [7] and in which they do not (for $R \geq$ Ho) [8], of course, having a strong impact on the magnetic properties of alloys also through R-Mn interactions. RNi$_2$ alloys have been investigated as potentially reversible hydrogen storage [9, 10]. A discussion on whether the Ni moment is (non-)zero in RNi$_2$ has continued for decades; finally, a non-zero moment was observed using microscopic methods [11, 12].

*Corresponding author: e-mail address: t.kovaliuk@mag.mff.cuni.cz

T a b l e 1. Characterization of samples $R_{1-y}Pd_{2+x+y}Mn_{1-x}$: initial composition, stoichiometry of the as-cast and annealed ingots; melting temperature T_{melt}; lattice parameter a of the cubic *Im-3m* structure (error based on the least-square refinement of peaks positions); paramagnetic Curie-Weiss temperature Θ_{CW}; effective magnetic moment μ_{eff}; the value of the magnetization in 9 T determined from $M(\mu_0 H)$ data measured at 4 and 100 K; the electronic specific heat coefficient γ, Debye coefficient β, and the Debye temperature Θ_D are presented

	$GdPd_2Mn$	$TbPd_2Mn$	$DyPd_2Mn$
Composition – initial	1.00 : 2.00 : 1.03	1.00 : 2.00 : 1.03	1.00 : 2.00 : 1.03
Composition – as-cast sample	inhomogeneous → → 0.81(2) : 2.09(1) : 1.10(1)	0.95(3) : 2.17(1) : 0.88(1)	0.93(3) : 2.14(2) : 0.93(1)
Composition – annealed sample	inhomogeneous	0.95(3) : 2.20(1) : 0.85(1)	1.00(3) : 2.15(1) : 0.85(1)
T_{melt} (K)	1126/1230(5)	1321(4)	1366(3)
a (Å)	–	3.374(2)	3.315(1)
Θ_{CW} (K)	–	–40(2)	–51(2)
μ_{eff} (μ_B)	–	9.63(3)	10.60(2)
μ_{9T}^{4K} (μ_B)	–	2.25(2)	2.98(2)
μ_{9T}^{100K} (μ_B)	–	1.42(2)	1.89(2)
γ(mJ mol^{-1} K^{-2})	–	11.6(3)	18.5(3)
β(mJ mol^{-1} K^{-4})	–	0.292(2)	0.284(2)
Θ_D (K)	–	71(1)	69(1)

During the ongoing research of RT_2 alloys, their physical properties have been tuned by substitutions (hundreds of publications). Significant attention has been dedicated to the RNi_2Mn alloys with R = Tb, Dy, Ho, and Er, e.g., [13–15]. The alloys crystallize in a cubic $MgCu_2$-type structure (C15, *Fd-3m*) identical to the RNi_2 Laves phase. Mn atoms are randomly distributed at the R and Ni positions (Wyckoff positions 8*a* and 16*d*, respectively); however, the Mn occupation of sites was reported not uniform – instead, the 8*a* site contains several percent of vacancies [13, 14]. The alloys with light R were not synthesized because of the highly different atomic radii of R and Mn, resulting in phase competition. A change in crystal structure was reported for high concentrations of Mn, e.g., to rhombohedral $PuNi_3$-type structure (*R-3m*) for RNi_2Mn_x alloys with R = Gd ($x > 0.4$), Tb ($x > 1.25$), Dy ($x > 1.5$), and Er ($x > 2$) [15–18]. The manganese content considerably affects the magnetic properties of the alloy; noticeably, the magnetic ordering temperature is multiple times higher than the RNi_2 analogues [14, 18]. Simultaneously, the magnetic moment and magnetostriction of the alloys decrease, and the coercive field increases with Mn substitution. Contrary to the small moment of Ni [19], which makes the R-R magnetic interaction by and large dominant in RNi_2, the Mn moment in RNi_2Mn is considerably larger (about 1.4 μ_B) [20, 21], and therefore the R-T and T-T interactions play a role. A noncollinear ferrimagnetic structure in RNi_2Mn (with R = Tb) was proposed based on magnetization and neutron diffraction studies [17].

The structural and magnetic properties of RNi_2Mn alloys have inspired further studies on RCo_2Mn counterparts. Similarly, a noticeable increase in ordering temperature and a decrease in the total magnetic moment with increasing Mn content have been reported [22, 23]. Moreover, by Mn doping, a tuneable thermal expansion from negative to positive was observed in this series [24]. Following these studies, we have synthesized and characterized, for the first time, the heavy rare earth RT_2Mn alloys with T = Pd having a larger atomic radius (= 1.37 Å, compared to 1.24 Å for T = Ni) whilst being isoelectronic with Ni.

2. Sample preparation and experimental details

Polycrystalline RPd_2Mn (R = Gd, Tb, Dy) alloys were prepared by arc-melting of the initial elements (Mn – 3N5 = 99.95 % purity (AlfaAesar), Pd – 4N5, Gd – 3N, Tb – 3N, Dy – 3N). 3 % of Mn was added to the content [25, 26]; the initial stoichiometry of the samples is listed in Table 1. The surface of the initial manganese pieces was etched with a dilute solution of nitric acid to remove any oxide layer before the initial weighting. Ingots of mass ∼ 1 g were remelted three times to ensure a good volume homogeneity of the samples. The mass loss of the samples was approximately 5 %. Based on the results presented below, Mn was heavily evaporated during the melting process.

The crystal structure, homogeneity, distribution of individual elements, and phase purity of synthesized samples were investigated employing X-ray diffraction (XRD) and electron microscopy. Part of the sample was ground and examined using a Bruker D8 diffractometer with Cu K_α radiation (Bragg-Brentano geometry, zero-diffraction Si plate as a holder). Rietveld analysis of the measured diffraction patterns was performed using the FullProf package [27]. Another part of the sample was polished and inspected by the scan-

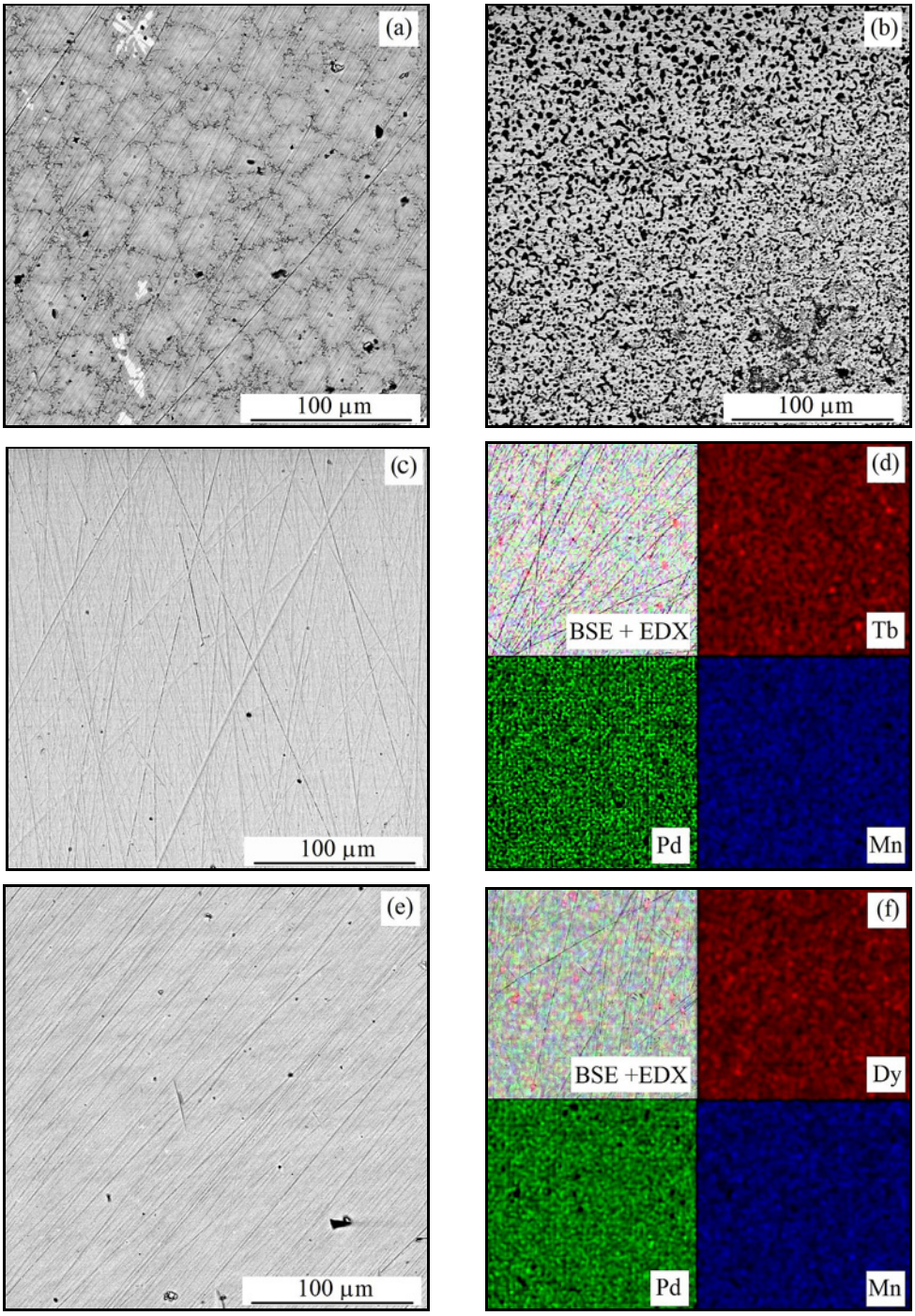

Fig. 1. Electron microscopy on RPd$_2$Mn. BSE images and EDX elemental maps are presented for (a) as-cast and (b) annealed R = Gd; (c, d) annealed R = Tb; and (e, f) annealed R = Dy samples, highlighting the increased homogeneity of samples after annealing.

ning electron microscope MIRA, Tescan, equipped with the backscattered electrons (BSE) detector and the energy-dispersive X-ray (EDX) analyser. The data were analysed using the Esprit software (corrections for atomic number, absorption, and fluorescence were done).

The melting temperature of the sample and any possible additional transitions in the high-temperature region were examined by differential scanning calorimetry (DSC) on a SETSYS Evolution 24 (SETARAM Instrumentation). Al_2O_3 crucibles with a lid were used as sample holders. The DSC data were measured on ~ 10 mg samples under He protective atmosphere at temperatures from 320 to 1420 K with the heating/cooling rate of 10 K min^{-1}. The melting temperature, T_{melt}, was determined as the onset of the

DSC peak corresponding to the first-order transition from solid to liquid phase (Table 1).

With knowledge of the melting temperature, the samples were annealed at temperature $T_{\mathrm{anneal}} = 1273\,\mathrm{K}$, approximately 50 K below T_{melt}. The ingots were wrapped in Ta foil and sealed under an Ar atmosphere in quartz glass tubes. The ingots were annealed for one week at constant temperature and subsequently quenched in cold water. No contamination of the Ta foil or quartz tubes was observed. The annealed samples were again investigated by XRD, BSE, and EDX.

Magnetization and specific heat were measured on a Physical Properties Measurement System (PPMS, Quantum Design) on ~ 200 and ~ 12 mg samples. The magnetization measurement was carried out using a vibrating sample magnetometer (VSM) insert at temperatures ranging from 1.8 to 400 K. Specific heat was measured using a standard time-relaxation method in the temperature range from 1.8 to 300 K.

3. Sample characterization

The quality of prepared samples, their purity and stoichiometry were investigated by electron microscopy and powder X-ray diffraction. BSE and EDX techniques revealed that the $TbPd_2Mn$ and $DyPd_2Mn$ are single-phase samples. However, their stoichiometry differs from the desired one $R:Pd:Mn = 1:2:1$; see Table 1. Pd-rich samples, slightly R- and considerably Mn-deficient samples, were synthesized. The stoichiometry deviation is also reflected by the samples' mass loss of approximately 5 %. The attempt to synthesize the $GdPd_2Mn$ alloy resulted in a highly inhomogeneous sample (Fig. 1). The results of the EDX analysis were confirmed by X-ray diffraction patterns (discussed below).

Subsequently, the prepared samples were measured by DSC. The inhomogeneity of the $GdPd_2Mn$ sample is also reflected in the DSC data (Fig. 2); several high-temperature peaks are observed. Notably, the corresponding peaks are also followed in the DSC data measured on cooling (indicating phase/s stability). Relatively sharp, individual peaks related to the solid-liquid transition in $TbPd_2Mn$ and $DyPd_2Mn$ data are observed. T_{melt} for individual compositions was determined and is listed in Table 1. Low-intensity peaks are traced at around 1050 and 1184 K in the DSC data for $TbPd_2Mn$ and at 982 K for $DyPd_2Mn$. We ascribe these peaks to the secondary phases in the samples, which are, nevertheless, present in relatively low amounts – they were not identified by EDX and XRD techniques within the resolution/background of these techniques. However, the peaks are not observed in the cooling data, suggesting their thermal instability and, therefore, the importance of the sample annealing.

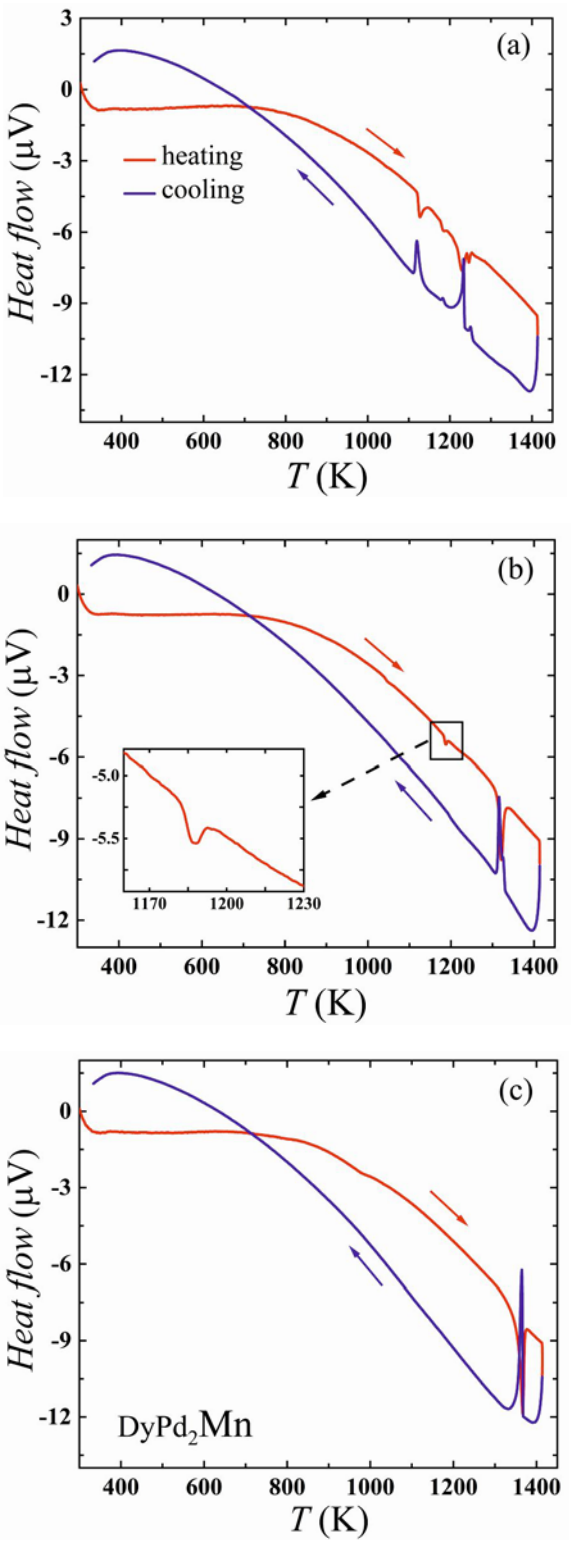

Fig. 2. DSC measurement on as-cast RPd_2Mn samples. The inset highlights minor intensity feature marked in the main panel ascribed to the impurity phase.

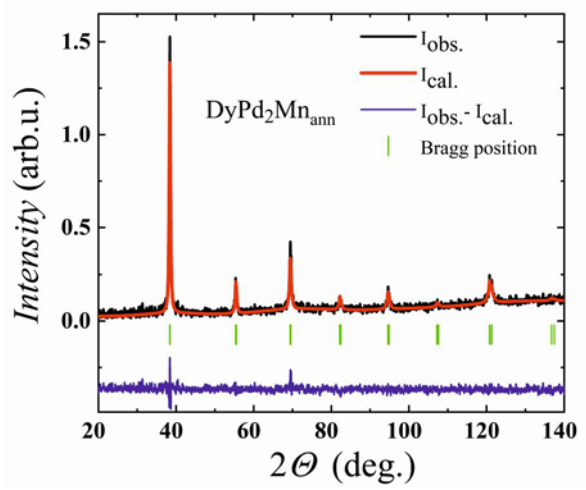

Fig. 3. Powder X-ray diffraction patterns of $DyPd_2Mn$. Fits the *Im-3m* model crystal structure (red line), difference curve (blue line), and Bragg positions (green marks) are presented.

Indeed, the annealing process slightly improved the quality/homogeneity of the $TbPd_2Mn$ and $DyPd_2Mn$ samples. The $GdPd_2Mn$ sample was also changed by annealing; however, it remained highly inhomogeneous (Fig. 1b). This sample was excluded from further investigation. The stoichiometry of the R = Tb and Dy members was influenced by annealing. The manganese content in the samples further decreased, notably to the same value for both members (Table 1). The stoichiometry of the samples $R_{1-y}Pd_{2+x+y}Mn_{1-x}$ is shifted from the ideal RPd_2Mn composition, similar to the RPd_2 (or $R_{10}Pd_{21}$) case [3]. The atomic radii of the constituent elements have a considerable impact on the actual stoichiometry and, as demonstrated below, on the crystal lattice of the RT_2Mn alloys.

4. Crystal structure of $TbPd_2Mn$ and $DyPd_2Mn$

The powder XRD patterns of the prepared samples are not consistent with the cubic C15 crystal structure, which has been reported for the analogues RNi_2Mn and RCo_2Mn. $TbPd_2Mn$ and $DyPd_2Mn$ are not ternary Laves phases. However, they cannot also be described by the monoclinic $Sm_{10}Pd_{21}$-type of structure (*C2/m*) reported for RPd_2 [3]. The XRD pattern for the $DyPd_2Mn$ sample is presented in Fig. 3, and the analysis leading to the identification of its crystal structure is provided:

(i) The Le Bail method was used to determine the lattice parameters and corresponding crystallographic system from the diffraction patterns. The five most intensive peaks from diffraction patterns were selected, and the Dicvol program [28] from the FullProf package [27] was employed for the structure analysis. The program suggested three sets of lattice parameters and crystallographic systems: a_c = 3.316 Å for the cubic system (holohedral space group *Pm3m*); a_h = 2.707 Å and c_h = 3.315 Å for the hexagonal system (holohedral space group *P6/mmm*); and a_t = 3.317 Å and c_t = 2.707 Å for the tetragonal system (holohedral space group *P4/mmm*). The suggested models were used to fit the diffraction patterns, and the agreement between the data and fit was evaluated. All three models describe all unambiguously observable (including low-intensity) peaks in the diffraction patterns. Of course, zero intensity in diffraction patterns at numerous reflections indicated by the model is observed since the holohedral groups have no systematic extinctions.

(ii) The space group describing the patterns was searched for using the CheckGroup program [27]. We note that the number of observable peaks in our diffraction patterns is relatively low for precise analysis. Naturally, the analysis was commenced with the cubic system as the most symmetrical one. Five non-centered space groups were suggested by the program, including the most symmetrical *Pm-3m* group. Fitting the diffraction pattern with this space group still showed many reflections without corresponding peaks in the data. Similar results were seen whilst testing the other suggested space groups. A centering of the lattice is necessary to reduce the number of reflections. Therefore, we tested supergroups of *Pm-3m* with fcc and bcc centering. Multiple additional reflections without corresponding peaks in the data were observed for the *Fm-3m* model (considering the lattice parameter 2 × a_c); $DyPd_2Mn$ does not belong among the so-called Heusler alloys, as seen when Mn is replaced by a larger radius *p*-block element [29]. The body-centered *Im-3m* space group describes all the measured peaks, and importantly, no additional reflections (without corresponding peaks in the data) are generated.

(iii) Determining the atomic positions of individual elements in a given space group is generally a non-trivial task. Several structure models – based on the formula unit, elements, and an occupational number of individual Wyckoff positions – have been devised and compared with the measured data (peak intensities). We started with the simplest model, a complete disorder of Dy, Pd, and Mn atoms on the single Wyckoff position 2*a*: (0, 0, 0). Almost perfect agreement is observed between the model (a = 3.315(1) Å) and the data.

A final fit of the model to the data was performed. Trials to fit the occupancies of individual elements on the 2*a* position failed. Therefore, the content of elements was fixed to the values determined by EDX analysis. The final fit of the data is presented in Fig. 3, and the refined lattice parameter is listed in Table 1. $TbPd_2Mn$ diffraction data were fitted to the same model, leading to a similar agreement (χ^2 = 2.2, com-

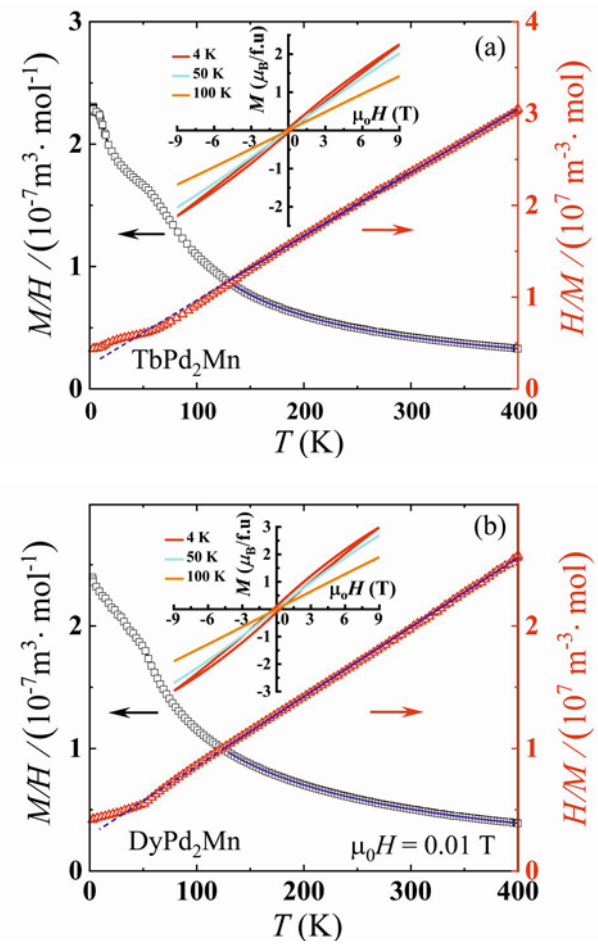

Fig. 4. Magnetization measurements on $TbPd_2Mn$ and $DyPd_2Mn$ alloys. The temperature dependence of magnetization $M/H(T)$ and its reciprocal value $H/M(T)$ are presented together with the fit to the Curie-Weiss law (within the 130–400 K interval; blue line) and its extrapolation to the low temperature (dashed line). Selected isothermal magnetization data are presented in the insets.

parable to $\chi^2 = 2.0$). We note that the diffraction patterns contain a relatively small number of peaks and high background, limiting our crystal structure determination. The uniform filling of a single site by three atoms with significantly different atomic numbers (atomic radii, atomic mass) is unusual. Nevertheless, based on the diffraction patterns, we have ruled out the crystal structures previously reported for related alloys (see section Introduction).

The complete atomic disorder on a single Wyckoff position in the *Im-3m* lattice makes it extremely difficult to understand and model the properties of the RPd$_2$Mn alloys quantitatively, and thus effective structure-property relations are challenging to obtain.

5. Magnetic and thermal properties

The physical properties of the samples were investigated by magnetization and specific heat measurements. The temperature dependence of magnetization reveals a standard paramagnetic response of $TbPd_2Mn$ and $DyPd_2Mn$ at a temperature from 400 K to approximately 130 K (or even down to approximately 70 K, considering the uncertainty of the measured data, Fig. 4). No clear indications of ferrimagnetic ordering (R-Mn coupling), reported for RNi$_2$Mn and RCo$_2$Mn analogues [14, 18], are observed in this temperature interval. The attempts to describe the inverse dc-magnetic susceptibility by the hyperbolic form of the Curie-Weiss law for two sublattices [30–32] failed due to the slight curvature of the H/M curves. The $H/M(T)$ dependence is described by a standard Curie-Weiss law with fitted paramagnetic Curie-Weiss temperatures, Θ_{CW}, and effective magnetic moment, μ_{eff}, listed in Table 1. The fitted values of μ_{eff} are strikingly close to those of the free ions of Tb^{3+} (9.72 μ_B) and Dy^{3+} (10.65 μ_B), indicating the paramagnetic state of the alloys and no significant Mn moment. The negative Curie-Weiss temperature suggests average antiferromagnetic exchange interactions. A bifurcation of zero field-cooled (ZFC) and field-cooled (FC) magnetization below approximately 70 K, presented in Fig. 5, is not typical for a purely antiferromagnetic material. We note that the temperature at which the ZFC and FC magnetization curves initially bifurcate is similar in $TbPd_2Mn$ and $DyPd_2Mn$. One can speculate that it is connected with the magnetic interactions between Mn moments and, in turn, with the R-Mn coupling. However, the Mn moments should also be manifested in higher-temperature magnetization data. That is, values of μ_{eff} should differ from (be higher than) the values of R^{3+} free ions. We cannot rule out a possible presence of secondary phase/s, namely RMn_2, although they were not observed by electron microscopy and X-ray diffraction. Both $TbMn_2$ and $DyMn_2$ reveal magnetic phase transition below about 40 K [33, 34], which is relatively close (about 20 K below) to the temperature of bifurcation of ZFC and FC magnetization curves. On the other hand, a second magnetic transition below 25 K in $DyMn_2$ [34] is not pronounced in the measured data.

In contrast, the $TbPd_2Mn$ magnetization data reveal a second, relatively sharp anomaly at around 10 K, which is not observed in the $DyPd_2Mn$ data. The anomaly might be connected with magnetic correlations between Tb-Tb, Tb-Mn, or Pd-Mn. A long-range magnetic ordering (antiferromagnetic type) is not expected, considering a complete disorder of constituent atoms on a single Wyckoff position. Alternatively, the presence of secondary phase/s, namely Pd-Mn alloys exhibiting ferromagnetic ordering at around 10 K [35], can be speculated about (not confirmed by the electron microscopy and X-ray diffraction measurements).

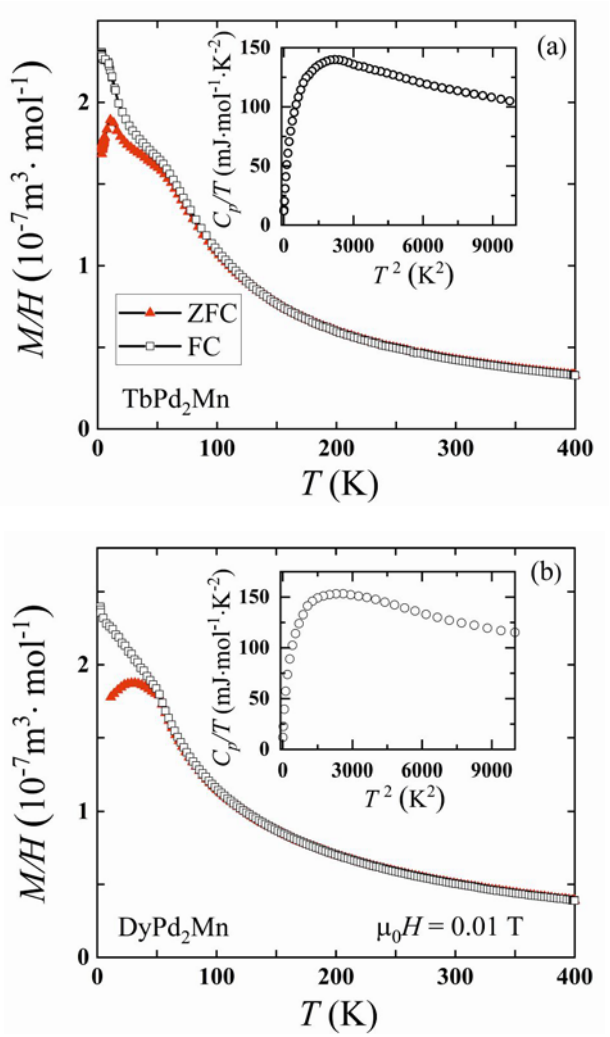

Fig. 5. Magnetization data measured under the ZFC and FC regimes in a magnetic field of 0.01 T. The insets contain the temperature evolution of the specific heat measured on the respective alloys.

Based on measured data, no unambiguous conclusion can be made.

The scenario of secondary phase(s) in the samples is supported by the specific heat measurements. A C_p/T vs T^2 plot is presented in the inset of Fig. 5. Only subtle anomalies are observed below 70 K. That is, any magnetic ordering of the RPd$_2$Mn alloys is not reproduced in the data. The low-temperature specific heat data (2–15 K) were analysed using the Sommerfield-Debye formula: $C_p(T) = \gamma T + \beta T^3$ with γ standing for the Sommerfield coefficient of electronic specific heat, and β is Debye lattice (electron–phonon) specific heat coefficient. The fitted parameters, including the Debye temperature calculated as $C_p = (12R\pi^4)/5(T/\Theta_D)^3$ [36], where R is gas constant, are similar for both alloys (listed in Table 1). Also, these parameters suggest that the two alloys do not magnetically order down to low temperatures. The anomalies in magnetization data (and weak anomalies in specific heat data) can be ascribed to secondary phase/s.

The possibility of a ferromagnetic ground state is mostly excluded in both alloys. The isothermal magnetization data (insets of Fig. 4) reveal hysteresis with a coercive field of about 0.24 T for TbPd$_2$Mn and 0.36 T for DyPd$_2$Mn at 4 K. However, the magnetization does not saturate in magnetic fields as high as 9 T. The magnetization value in 9 T is significantly lower (Table 1) than the spontaneous magnetic moment expected for rare earth ions (9 μ_B for Tb^{3+} and 10 μ_B for Dy^{3+}). Hence, ferrimagnetic ordering can be speculated about. Nevertheless, the apparent complete atomic disorder (on 2a Wyckoff site), significant off-stoichiometry, and the probable presence of secondary phase/s strongly affect the low-temperature (< 70 K) magnetic properties of the investigated samples, making their interpretation ambiguous.

6. Conclusions

Non-stoichiometric, considerably Mn-deficient ($x = 0.15$), $R_{1-y}Pd_{2+x+y}Mn_{1-x}$ samples with R = Tb and Dy were synthesized and characterized. The synthesis of the R = Gd analogue failed, demonstrating the difficulties in preparing new RT_2Mn alloys; that is, the significance of the atomic radii ratio of constituent elements. Unlike the analogous alloys RNi$_2$Mn and RCo$_2$Mn crystallizing in a C15 type of structure (*Fd-3m*), the crystal structure of the investigated samples was determined to be fully disordered: R, Pd, and Mn atoms randomly distributed over the 2a Wyckoff position of the W-type structure (A2, bcc, *Im-3m*). The samples remained paramagnetic down to at least 130 K. Negative Curie-Weiss paramagnetic temperature and effective magnetic moment noticeably close to the value expected for free rare-earth ions were refined. No contribution of Mn magnetism was traced. A bifurcation between ZFC and FC magnetization below 70 K could be ascribed to magnetic correlations between R or/and Mn moments, particularly in the case of R = Tb where additional ZFC--FC splitting is observed below an additional anomaly at 10 K. Possible ferrimagnetic ordering/interactions were supported by isothermal magnetization data. However, the confident explanation of magnetization data remains ambiguous considering the atomic disorder (frozen metastable phases are investigated, 3rd law of thermodynamics) and non-stoichiometry of the investigated samples. Moreover, the possible presence of secondary phase/s, although they were not directly observed investigating the samples employing electron microscopy and X-ray diffraction methods, could also explain the observed bifurcation.

Acknowledgements

This work was supported by the Czech Ministry of Education, Youth and Sports through Project MATFUN – CZ.02.1.01/0.0/0.0/15_003/0000487. The sample preparation and characterization were performed in MGML (http://mgml.eu), supported by the Czech Research Infrastructures program (project no. LM2023065). The work of TK and RHC was supported by the Czech Science Foundation (grant no. 22-22063S).

References

[1] V. Franco, J. S. Blázquez, J. J. Ipus, J. Y. Law, L. M. Moreno-Ramírez, and A. Conde, Magnetocaloric effect: From materials research to refrigeration devices, Progress in Materials Science 93 (2018) 112–232. https://doi.org/10.1016/j.pmatsci.2017.10.005

[2] J. H. Zhu, C. T. Liu, L. M. Pike, P. K. Liaw, A thermodynamic interpretation of the size-ratio limits for laves phase formation, Metallurgical and Materials Transactions 30 A (1999) 1449–1452. https://doi.org/10.1007/s11661-999-0292-5

[3] P. Manfrinetti, A. Provino, N. S. Sangeetha, and S. K. Dhar, The $R_{10}Pd_{21}$ compounds (R = Y, Pr, Nd, Sm, Gd-Lu), Crystal structure and magnetism of the RPd_2 phases, Journal of Materials Chemistry C 6 (2018) 5250–5260. https://doi.org/10.1039/C8TC00160J

[4] F. Stein and A. Leineweber, Laves phases: a review of their functional and structural applications and an improved fundamental understanding of stability and properties, Journal of Materials Science 56 (2021) 5321–5427. https://doi.org/10.1007/s10853-020-05509-2

[5] P. Wikus, E. Canavan, S. T. Heine, K. Matsumoto, T. Numazawa, Magnetocaloric materials and the optimization of cooling power density, Cryogenics 62 (2014) 150–162. https://doi.org/10.1016/j.cryogenics.2014.04.005

[6] J. L. Sánchez Llamazares, J. Zamora, C. F. Sánchez-Valdés, P. Álvarez-Alonso, Design and fabrication of a cryogenic magnetocaloric composite by spark plasma sintering based on the RAl_2 laves phases (R = Ho, Er), Journal of Alloys and Compounds 831 (2020) 154779. https://doi.org/10.1016/j.jallcom.2020.154779

[7] K. Yoshimura and Y. Nakamura, NMR study of magnetic state of Mn IN Y-Mn intermetallic compounds, Journal of Magnetism and Magnetic Materials 40 (1983) 55–60. https://doi.org/10.1016/0304-8853(83)90010-0

[8] H. Wada, H. Nakamura, K. Yoshimura, M. Shiga, and Y. Nakamura, Stability of Mn moments and spin fluctuations in RMn_2 (R:Rare earth), Journal of Magnetism and Magnetic Materials 70 (1987) 134–136. https://doi.org/10.1016/0304-8853(87)90380-5

[9] K. Aoki, T. Yamamoto, T. Masumoto, Hydrogen induced amorphization in RNi_2 Laves phases, Scripta Metallurgica 21 (1987) 27–31. https://doi.org/10.1016/0036-9748(87)90401-7

[10] S. Zhao, H. Wang, J. Liu, Exploring the hydrogen-induced amorphization and hydrogen storage reversibility of $Y(Sc)_{0.95}Ni_2$ laves phase compounds, Materials 14 (2021) 1–9. https://doi.org/10.3390/ma14020276

[11] M. Mizumaki, K. Yano, I. Umehara, F. Ishikawa, K. Sato, A. Koizumi, N. Sakai, T. Muro, Verification of Ni magnetic moment in (formula presented) Laves phase by magnetic circular dichroism measurement, Physical Review B – Condensed Matter and Materials Physics 67 (2003) 132404. https://doi.org/10.1103/PhysRevB.67.132404

[12] K. Yano, Y. Tanaka, I. Matsumoto, I. Umehara, K. Sato, H. Adachi and H. Kawata, Detection of Ni magnetic moment in $GdNi_2$ compound by magnetic Compton profile (MCP) method, Journal of Physics Condensed Matter 18 (2006) 6891–6895. https://doi.org/10.1088/0953-8984/18/29/026

[13] J. L. Wang, C. C. Tang, G. H. Wu, Q. L. Liua, N. Tang, W. Q. Wang, W. H. Wang, F. M. Yang, J. K. Liang, F. R. de Boer, K. H. J. Buschow, Structure and magneto-history behavior of $DyNi_2Mn$, Solid State Communications 121 (2002) 615–618. https://doi.org/10.1016/S0038-1098(02)00041-8

[14] J. L. Wang, C. Marquina, M. R. Ibarra, G. H. Wu, Structure and magnetic properties of RNi_2 Mn compounds (R = Tb, Dy, Ho, and Er), Physical Review B – Condensed Matter and Materials Physics 73 (2006) 094436. https://doi.org/10.1103/PhysRevB.73.094436

[15] A. Aryal, A. Quetz, S. Pandey, T. Samanta, I. Dubenko, D. Mazumdar, S. Stadler, N. Ali, Phase transitions and magnetocaloric and transport properties in off-stoichiometric $GdNi_2Mn_x$, Journal of Applied Physics 119 (2016) 043905. http://dx.doi.org/10.1063/1.4940877

[16] E. G. Gerasimov, N. V. Mushnikov, P. B. Terentev, V. S. Gaviko, A. A. Inishev, Magnetic properties of the off-stoichiometric $GdNi_2Mn_x$ alloys, Journal of Alloys and Compounds 571 (2013) 132–137. https://doi.org/10.1016/j.jallcom.2013.03.233

[17] N. V. Mushnikov, V. S. Gaviko, E. G. Gerasimov, P. B. Terent'ev, I. A. Tkach, Magnetic properties and structure of nonstoichiometric rare-earth transition-metal intermetallic compounds $TbNi_2Mn_x$ ($0 \leq x \leq 1.5$), The Physics of Metals and Metallography 110 (2010) 210–217. https://doi.org/10.1134/S0031918X10090036

[18] N. V. Mushnikov, E. G. Gerasimov, P. B. Terentev, V. S. Gaviko, A. A. Inishev, Magnetic properties of nonstoichiometric 4f–3d intermetallics, Physics of Metals and Metallography 120 (2019) 1347–1353. https://doi.org/10.1134/S0031918X19130180

[19] T. V. Kuznetsova, V. I. Grebennikov, E. G. Gerasimov, N. V. Mushnikov, Electronic magnetic structure of intermetallic compounds RNi_2Mn studied by XMCD, Journal of Magnetism and Magnetic Materials 440 (2017) 50–53. https://doi.org/10.1016/j.jmmm.2016.12.083

[20] N. V. Mushnikov, V. S. Gaviko, J. Park, A. N. Pirogov, Crystal and magnetic structure of $TbNi_2Mn$, Physical Review B – Condensed Matter and Materials Physics 79 (2009) 84419. https://doi.org/10.1103/PhysRevB.79.184419

[21] V. V. Marchenkov, N. V. Mushnikov, T. V. Kuznetsova, A. Buling, E. G. Gerasimov, V. S. Gaviko,

V. I. Grebennikov, K. A. Fomina, H. W. Weber, C. Derks, Electrical, magnetic properties and electronic structure of non-stoichiometric $DyNi_2Mn_x$ compounds, Journal of Physics: Conference Series 400 (2012) 032050. https://doi.org/10.1088/1742-6596/400/3/032050

[22] B. Maji, K. G. Suresh, A. K. Nigam, Magnetic and electrical properties of RCo_2Mn (R = Ho, Er) compounds, Journal of Magnetism and Magnetic Materials 322 (2010) 2415–2418. https://doi.org/10.1016/j.jmmm.2010.02.048

[23] E. G. Gerasimov, A. A. Inishev, P. B. Terentev, V. A. Kazantsev, N. V. Mushnikov, Magnetostriction and thermal expansion of nonstoichiometric $TbCo_2Mn_x$ compounds, Journal of Magnetism and Magnetic Materials 523 (2021) 167628. https://doi.org/10.1016/j.jmmm.2020.167628

[24] C. S. Fang, J. Li Wang, W. D. Hutchison, W. Q. Wang, A. J. Studer, Q. F. Gu, J. Zhao, Controllable isotropic thermal expansion in series of designed magnetocaloric materials $HoCo_2Mn_x$ (x = 0–1.0), Journal of Alloys and Compounds 863 (2021) 158063. https://doi.org/10.1016/j.jallcom.2020.158063

[25] T. Kovaliuk, B. Vondráčková, J. Valenta, R. H. Colman, and M. Klicpera, Evolution of magnetic and structural phase transitions in solid solutions $Ni_2MnGa_{1-x}Ge_x$, Journal of Alloys and Compounds 894 (2022) 162441. https://doi.org/10.1016/j.jallcom.2021.162441

[26] M. Klicpera, M. Kratochvílová, F. Malý, T. Kovaliuk, J. Valenta, R. H. Colman, Systematic search for new Co_2YZ and Rh_2YZ Heusler alloys based on theoretical calculations, Intermetallics 130 (2021) 107060. https://doi.org/10.1016/j.intermet.2020.107060

[27] J. Rodriguez-Carvajal, Recent advances in magnetic structure determination neutron powder diffraction, Physica B: Condensed Matter 192 (1993) 55–69. https://doi.org/10.1016/0921-4526(93)90108-I

[28] A. Boultif, D. Louër, Powder pattern indexing with the dichotomy method, Journal of Applied Crystallography 37 (2004) 724–731. https://doi.org/10.1107/S0021889804014876

[29] A. E. Dwight, C.W. Kimball, ScT_2X and LnT_2X compounds with the $MnCu_2$ Al-type structure, Journal of the Less Common Metals 127 (1987) 179–182. https://doi.org/10.1016/0022-5088(87)90376-6

[30] J. S. Smart, The Néel Theory of Ferrimagnetism, American Journal of Physics 23 (1955) 356–370. https://doi.org/10.1119/1.1934006

[31] R. N. Bhowmik, R. Ranganathan, R. Nagarajan, Lattice expansion and noncollinear to collinear ferrimagnetic order in a $MnCr_2O_4$ nanoparticle, Physical Review B – Condensed Matter and Materials Physics 73 (2006) 144413. https://doi.org/10.1103/PhysRevB.73.144413

[32] H. Chang, Y. Q. Guo, J. K. Liang, G. H. Rao, Magnetic ordering and irreversible magnetization between ZFC and FC states in RCo_5Ga_7 compounds, Journal of Magnetism and Magnetic Materials 278 (2004) 306–310. https://doi.org/10.1016/j.jmmm.2003.12.1316

[33] E. Talik, M. Kulpa, T. Mydlarz, J. Kusz, H. Böhm, A. Winiarski, Magnetic properties of the $TbMn_2$ single crystals, Physica B: Condensed Matter 271 (1999) 265–272. https://doi.org/10.1016/S0921-4526(99)00206-9

[34] E. Talik, M. Kulpa, T. Mydlarz, J. Kusz, H. Böhm, Magnetic properties of $DyMn_2$ single crystals, Journal of Alloys and Compounds 308 (2000) 30–37. https://doi.org/10.1016/S0925-8388(00)00873-2

[35] R. E. Parra, A. C. Gonzalez, R. A. Lopez, Ferromagnetism and atomic short-range order in dilute PdMn alloys, Journal of Physics: Condensed Matter 2 (1990) 7309–7315. https://doi.org/10.1088/0953-8984/2/35/006

[36] D. W. Rogers, Six. The Debye Equation. Einstein's Other Theory: The Planck-Bose-Einstein Theory of Heat Capacity, Princeton: Princeton University 2005, pp. 77–93. https://doi.org/10.1515/9780691216409-007